Available online at www.sciencedirect.com
SCIENCE DIRECT®
Physica A 323 (2003) 413–427
PHYSICA A
www.elsevier.com/locate/physa

Pair distribution of ions in Coulomb crystals

A.I. Chugunov[a], D.A. Baiko[a], D.G. Yakovlev[a,*], H.E. De Witt[b], W.L. Slattery[c]

[a] *Ioffe Physical-Technical Institute, 194021 St.-Petersburg, Russia*
[b] *Lawrence Livermore National Laboratory, Livermore, CA 94550, USA*
[c] *Los Alamos National Laboratory, Los Alamos, NM 87545, USA*

Received 27 September 2002

Abstract

The pair distribution function $g(\boldsymbol{r})$ of ions in body-centered-cubic and face-centered-cubic Coulomb crystals is calculated using the harmonic-lattice (HL) approximation in a wide temperature range, from the high-temperature classical regime ($T \gg \hbar\omega_p$, ω_p is the ion plasma frequency) to the low-temperature quantum regime ($T \ll \hbar\omega_p$). The radial pair distribution function $g(r)$ is calculated by averaging $g(\boldsymbol{r})$ over orientations of $\boldsymbol{r}$. In the classical limit, $g(r)$ is also obtained from extensive Monte Carlo (MC) simulations. MC and HL results are shown to be in good agreement. With decreasing temperature T, the correlation peaks of $g(\boldsymbol{r})$ and $g(r)$ become narrower and finally freeze at $T \ll \hbar\omega_p$ being solely determined by zero-point ion vibrations.

PACS: 52.27.Lw; 52.27.Gr

Keywords: Coulomb crystals; Correlations

1. Introduction

A model of a Coulomb crystal of point charges in a uniform neutralizing background of opposite sign is widely used in solid-state physics for describing electron–hole plasma (e.g., Ref. [1]), in plasma physics for describing dusty plasmas and ion plasmas in Penning traps (e.g., Ref. [2]); it is also used in astrophysics for describing crystals of ions in the cores of white dwarfs and the envelopes of neutron stars (e.g., Ref. [3]).

* Corresponding author.
E-mail address: yak@astro.ioffe.rssi.ru (D.G. Yakovlev).

0378-4371/03/$ - see front matter
doi:10.1016/S0378-4371(02)02027-7

To be specific, we consider a crystal of ions in a uniform electron background. We focus on correlation properties of ions described by the pair distribution function $g(\boldsymbol{r}) \equiv g(x,y,z)$ [the relative probability to find two ions at a distance $\boldsymbol{r}$; a formal definition is given by Eq. (5) below] and by the radial pair distribution function $g(r)$ obtained from $g(\boldsymbol{r})$ by averaging over orientations of $\boldsymbol{r}$.

Both functions, $g(\boldsymbol{r})$ and $g(r)$, are important for calculating various thermodynamic and kinetic properties of the crystals. For instance, they determine Coulomb energy of the system and provide the basis for a strict description of the processes involving ions. As an example, we can mention the problem of calculating nuclear reaction rates in dense stellar matter where the ions are arranged in Coulomb lattice (e.g., Ref. [4]). Under these conditions, the penetration of the Coulomb barrier takes place in the pycnonuclear or thermally excited pycnonuclear regimes being extremely sensitive to correlations (to pair distribution functions) of reacting ions. The problem has been solved under some simplifying assumptions and the main features have been understood, but the exact solution has not been derived so far. Moreover, the Fourier transforms of the pair distribution functions, the structure factors [see Eq. (1)], are needed to calculate, for instance, electron scattering rates in the Coulomb crystals and associated electron transport properties (e.g., Refs. [5–7]).

In principle, $g(\boldsymbol{r})$ and $g(r)$ can be determined numerically: by classical Monte Carlo (MC; e.g., Ref. [8], and references therein), molecular dynamics (MD; e.g., Ref. [9]), and also by path-integral Monte Carlo (PIMC; e.g., Ref. [10]). The results of these studies are very impressive, but the numerical methods are time consuming and require the most powerful computers. So far, accurate calculations of $g(r)$ have been performed only by MC for classical body-centered-cubic (bcc) and face-centered-cubic (fcc) Coulomb crystals ($T \gg \hbar\omega_p$) at $r/a \lesssim 7$, where $\omega_p = \sqrt{4\pi e^2 Z^2 n/M}$ is the ion plasma frequency, $a = (4\pi n/3)^{-1/3}$ is the ion sphere radius, Ze is the ion charge, M is its mass, and n is the number density. Accurate MC calculations of $g(\boldsymbol{r})$ in the classical regime would be straightforward but they would require much more computer resources (because of very pronounced peak structure of $g(\boldsymbol{r})$, see Section 3). They have not been performed so far, to the best of our knowledge.

Recently, Baiko et al. [6,11] constructed a semi-analytic model for calculating correlation properties of Coulomb crystals (dynamic and static structure functions as well as pair distribution functions) based on the harmonic lattice (HL) approximation (e.g., Ref. [12]). This model is much simpler for practical realization. It does not take into account ion statistics (exchange terms) but describes correctly other quantum effects.

In Ref. [11] the radial distribution function $g(r)$ given by the HL model was compared with MC results for classical bcc crystals ($T \gg \hbar\omega_p$), and the agreement turned out to be very good for $1.5 \lesssim r/a \lesssim 7.3$. In addition, the HL $g(r)$ was calculated for a quantum bcc crystal at one particular temperature $T = 0.1\hbar\omega_p$.

In this paper we present the results of HL calculations of $g(\boldsymbol{r})$ and $g(r)$ for bcc and fcc crystals. We obtain also new, more accurate, MC $g(r)$ for classical crystals and confirm good agreement with the HL model. Furthermore, we analyze the HL $g(\boldsymbol{r})$ and $g(r)$ in the quantum and intermediate (classical–quantum) regimes.

2. Formalism

Let us remind the main expressions of the HL approximation (e.g., Refs. [12,6,11]). We stress that the HL formalism has been known for a long time (e.g., Ref. [12]). We discuss here its implementation for Coulomb crystals. As can be shown, for instance, from Eqs. (6) and (9) of Ref. [6], the static ion–ion structure factor can be written as

$$S(\boldsymbol{k}) = \sum_{\boldsymbol{R}} \mathrm{e}^{\mathrm{i}\boldsymbol{k}\cdot\boldsymbol{R} - 2W(k) + v_{\alpha\beta}(\boldsymbol{R})k_\alpha k_\beta} - (2\pi)^3 n\delta(\boldsymbol{k}) \,, \tag{1}$$

where the sum is over direct lattice vectors $\boldsymbol{R}$, and $\mathrm{e}^{-2W(k)}$ is the Debye–Waller factor. The functions $W(k)$ and $v_{\alpha\beta}(\boldsymbol{R})$ can be expressed as

$$W(k) = \frac{3\hbar}{2M}\left\langle \frac{(\boldsymbol{k}\cdot\boldsymbol{e}_v)^2}{\omega_v}\left(\bar{n}_v + \frac{1}{2}\right)\right\rangle_{\mathrm{ph}} = \frac{\hbar k^2}{2M}\left\langle \frac{1}{\omega_v}\left(\bar{n}_v + \frac{1}{2}\right)\right\rangle_{\mathrm{ph}} \,, \tag{2}$$

$$v_{\alpha\beta}(\boldsymbol{R}) = \frac{3\hbar}{2M}\left\langle \frac{e_{v\alpha}e_{v\beta}}{\omega_v \tanh(z_v/2)}\,\mathrm{e}^{\mathrm{i}\boldsymbol{q}\cdot\boldsymbol{R}}\right\rangle_{\mathrm{ph}} \,. \tag{3}$$

In this case, $v \equiv (\boldsymbol{q}, s)$ labels phonon branches; $\boldsymbol{q}$, $\boldsymbol{e}_v$, and ω_v are, respectively, phonon wave vector (in the first Brillouin zone), polarization vector and frequency (to be determined from the standard dynamic-matrix equation); $\bar{n}_v = (\mathrm{e}^{z_v} - 1)^{-1}$ is the mean number of phonons in a mode v, $z_v = \hbar\omega_v/T$. The brackets

$$\langle f_v\rangle_{\mathrm{ph}} = \frac{1}{24\pi^3 n}\sum_{s=1}^{3}\int \mathrm{d}\boldsymbol{q}\, f_v \tag{4}$$

denote averaging over the phonon spectrum, which can be performed numerically, e.g., Refs. [13,5]; the integral is taken over the first Brillouin zone. The last equality in Eq. (2) is exact at least for bcc and fcc crystals. For these crystals, $W(k) = r_T^2 k^2/6$, where r_T^2 is the mean squared displacement of an ion in a lattice site.

Our main goal is to study the ion pair distribution function

$$g(\boldsymbol{r}) = 1 + \frac{1}{n}\int \frac{\mathrm{d}\boldsymbol{k}}{(2\pi)^3}\,[S(\boldsymbol{k}) - 1]\,\mathrm{e}^{-\mathrm{i}\boldsymbol{k}\cdot\boldsymbol{r}} \,. \tag{5}$$

Using Eq. (1) we have

$$g(\boldsymbol{r}) = \frac{1}{n}{\sum_{\boldsymbol{R}}}' \int \frac{\mathrm{d}\boldsymbol{k}}{(2\pi)^3}\,\mathrm{e}^{\mathrm{i}\boldsymbol{k}\cdot(\boldsymbol{R}-\boldsymbol{r}) - 2W(k) + v_{\alpha\beta}(\boldsymbol{R})k_\alpha k_\beta} \,. \tag{6}$$

The prime over the sum means that the central ($\boldsymbol{R} = 0$) lattice vector is excluded. At this stage it is natural to introduce the matrix $V_{\alpha\beta}(\boldsymbol{R}) = r_T^2\,\delta_{\alpha\beta}/3 - v_{\alpha\beta}(\boldsymbol{R})$ and its inverse: $N_{\alpha\beta}(\boldsymbol{R}) = (V^{-1})_{\alpha\beta}$. We can integrate then over $\boldsymbol{k}$ and obtain an analytic expression:

$$g(\boldsymbol{r}) = {\sum_{\boldsymbol{R}}}' \frac{\sqrt{N(\boldsymbol{R})}}{8\pi^{3/2} n}\,\mathrm{e}^{-N_{\alpha\beta}(\boldsymbol{R})(R_\alpha - r_\alpha)(R_\beta - r_\beta)/4} \,, \tag{7}$$

where $N(\boldsymbol{R})=\det\{N_{\alpha\beta}(\boldsymbol{R})\}$. This expression is convenient for numerical evaluation. Under the conditions, at which the present approach is valid (neglect of exchange terms), $g(\boldsymbol{r})$ is the sum of Gaussian peaks centered at direct lattice vectors, $\boldsymbol{R}$. The peaks should be narrow and should not essentially overlap. The major axes $\boldsymbol{n}_i$, $i=1,2,3$, of the Gaussian distribution for any peak at $\boldsymbol{r}\approx\boldsymbol{R}$ are the major axes of $N_{\alpha\beta}(\boldsymbol{R})$ ($N_{\alpha\beta}(\boldsymbol{R})n_{i\beta}=N_i(\boldsymbol{R})n_{i\alpha}$, with $\boldsymbol{n}_i\cdot\boldsymbol{n}_k=\delta_{ik}$). They are also the major axes of the initial matrix $v_{\alpha\beta}(\boldsymbol{R})$. The peak widths along the major axes are determined by the associated eigenvalues $N_i(\boldsymbol{R})$ (i.e., a width in the direction $\boldsymbol{n}_i$ is $\propto 1/\sqrt{N_i(\boldsymbol{R})}$). Notice also that $N(\boldsymbol{R})=N_1(\boldsymbol{R})N_2(\boldsymbol{R})N_3(\boldsymbol{R})$.

For many problems, it is important to introduce the radial pair distribution function

$$g(r)=\frac{1}{4\pi}\int \mathrm{d}\Omega\, g(\boldsymbol{r})=\sum_{\boldsymbol{R}}{}' g_{\boldsymbol{R}}(r)\,, \tag{8}$$

where $\mathrm{d}\Omega$ is the solid angle element in the direction of $\boldsymbol{r}$, and $g_{\boldsymbol{R}}(r)$ is the contribution from an ion in a lattice site $\boldsymbol{R}$. The latter contribution is non-negligible only if r is close enough to R. To find $g_{\boldsymbol{R}}(r)$ we must integrate the $\boldsymbol{R}$th term in (7) over orientations of $\boldsymbol{r}$ on a sphere of radius r. It is clear that only a small part of the spherical surface contributes to the integral, where $\boldsymbol{r}\approx\boldsymbol{R}$. While integrating, we can neglect the curvature of the spherical surface, and approximate this part of the surface by a plane which is perpendicular to the vector $r\hat{\boldsymbol{R}}$ and touches the end of this vector ($\hat{\boldsymbol{R}}$ is the unit vector directed along $\boldsymbol{R}$). In the exponent argument of the integrand, we may introduce $\boldsymbol{u}=\boldsymbol{r}-\boldsymbol{R}=\boldsymbol{u}_0+\Delta\boldsymbol{u}$, where $\boldsymbol{u}_0=(r-R)\,\hat{\boldsymbol{R}}$ and $\Delta\boldsymbol{u}$ lies in the integration plane (perpendicular to $\boldsymbol{R}$). It is convenient to introduce a 2D tensor $L_{ij}=N_{ij}$, where i and j refer to two arbitrary orthogonal axes ($i,j=1,2$) in the integration plane. Thus, L_{ij} represents the projection of $N_{\alpha\beta}$ onto the integration plane. Let us also introduce the major orthogonal axes of L_{ij} in the integration plane. They are defined by the orthogonal unit vectors $\boldsymbol{l}^{(k)}$, $k=1$ and 2, which lie in the integration plane and diagonalize L_{ij}: $L_{ij}l_j^{(k)}=L^{(k)}l_i^{(k)}$ ($L^{(k)}$ is an eigenvalue of L_{ij}). The integration then yields

$$g_{\boldsymbol{R}}(r)=\frac{\sqrt{N}}{8\pi r^2 n\sqrt{\pi L^{(1)}L^{(2)}}}\exp\left(-\frac{\tilde{u}_{0\alpha}N_{\alpha\beta}\tilde{u}_{0\beta}}{4}\right)\,, \tag{9}$$

where $\tilde{\boldsymbol{u}}_0=\boldsymbol{u}_0-\sum_k(l_\alpha^{(k)}N_{\alpha\beta}u_{0\beta})\,\boldsymbol{l}^{(k)}/L^{(k)}$.

Note one important limiting case in which $v_{\alpha\beta}(\boldsymbol{R})=v_0(\boldsymbol{R})\,\delta_{\alpha\beta}$. In this case $V_{\alpha\beta}(\boldsymbol{R})=V_0(\boldsymbol{R})\,\delta_{\alpha\beta}$, with $V_0(\boldsymbol{R})=r_T^2/3-v_0(\boldsymbol{R})$. The tensors $N_{\alpha\beta}(\boldsymbol{R})$ and $L_{ik}(\boldsymbol{R})$ also become isotropic, and Eq. (9) reduces to

$$g_{\boldsymbol{R}}(r)=\frac{1}{8\pi n r^2\sqrt{\pi V_0(\boldsymbol{R})}}\exp\left[-\frac{(R-r)^2}{4V_0(\boldsymbol{R})}\right]\,. \tag{10}$$

Baiko et al. [11] proposed another algorithm of calculating $g(r)$. Their Eqs. (14) and (15) are more general since they do not neglect the curvature of the integration surface. A careful examination of these equations shows that several terms are canceled

out, so that their $g_{\boldsymbol{R}}(r)$ can be written as

$$g_{\boldsymbol{R}}(r) = \frac{\sqrt{\pi}}{(2\pi)^3 rn} \sum_{\sigma=\pm 1} \int \frac{\mathrm{d}\Omega_{\boldsymbol{k}}}{x^2}\, \gamma \mathrm{e}^{-\gamma^2}\ , \tag{11}$$

where $\gamma = (r + \sigma R\mu)/x$, $\mu = \cos\vartheta$, ϑ is an angle between $\boldsymbol{k}$ and $\boldsymbol{R}$, $x^2 = 4k_\alpha V_{\alpha\beta}(\boldsymbol{R})k_\beta/k^2$, and $\mathrm{d}\Omega_{\boldsymbol{k}}$ is the solid angle element in the direction of $\boldsymbol{k}$.

Thus $g(r)$ can be calculated from Eq. (8) with $g_{\boldsymbol{R}}(r)$ taken either from Eq. (9) or from (11). The first algorithm is much more efficient (does not require 2D integration) and will be used below. Both algorithms give almost the same results in all physically reasonable cases we have checked.

The functions $g(\boldsymbol{r})$ and $g(r)$ depend on the lattice type and on two parameters: the classical ion-coupling parameter $\Gamma = Z^2e^2/(aT)$ and the quantum parameter $\theta = \hbar\omega_p/T$ that measures the importance of zero-point lattice vibrations. In addition, it is useful to introduce a density parameter. The most familiar density parameter is $R_\mathrm{s} = a/a_\mathrm{B}$, where $a_\mathrm{B} = \hbar^2/(Z^2e^2M)$ is the ion Bohr radius. However, we find more convenient to introduce another parameter $\Gamma_\mathrm{q} = Z^2e^2/(a\hbar\omega_p) = (R_\mathrm{s}/3)^{1/2}$ which is similar to the standard ion-coupling parameter Γ but with $\hbar\omega_p$ instead of the thermal energy T in the denominator. With this definition, $\Gamma = \Gamma_\mathrm{q}\theta$.

3. 3D pair distribution

In this section we analyze the results of HL calculations of $g(\boldsymbol{r})$ from Eq. (7). Figs. 1 and 2 show $g(\boldsymbol{r})$ for classical fcc and bcc Coulomb crystals at $\Gamma = 180$ (i.e., close to the melting value $\Gamma_\mathrm{melt} \approx 175$; see, e.g., Ref. [14]). In both figures, $\boldsymbol{r}$ varies in the planes containing lattice sites. One can observe Gaussian correlation peaks

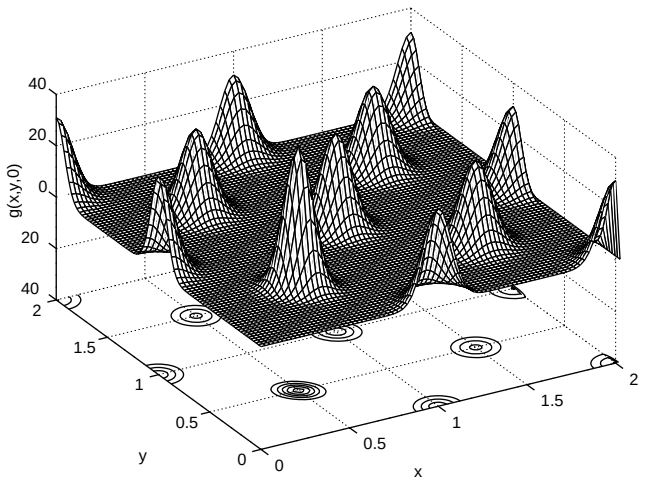

Fig. 1. $g(\boldsymbol{r})$ as a function of x and y in units of basic cube lengths at $z = 0$ for a classical fcc crystal at $\Gamma = 180$. The bottom plane shows isolines of $g(\boldsymbol{r})$.

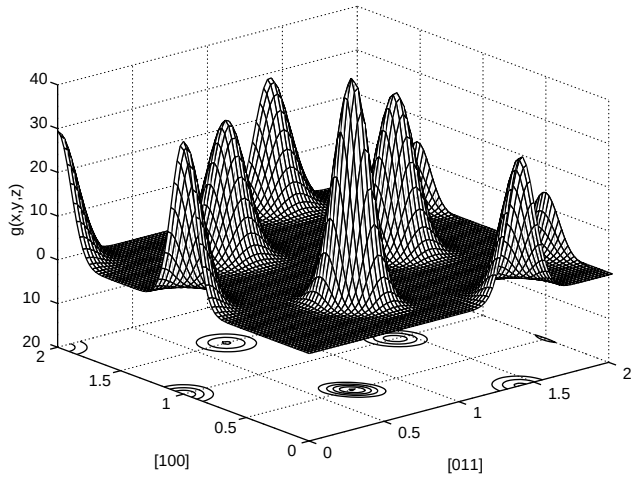

Fig. 2. $g(\boldsymbol{r})$ in the plane formed by two indicated directions (in units of basic cube lengths) for a classical bcc crystal at $\Gamma = 180$. The bottom plane shows isolines of $g(\boldsymbol{r})$.

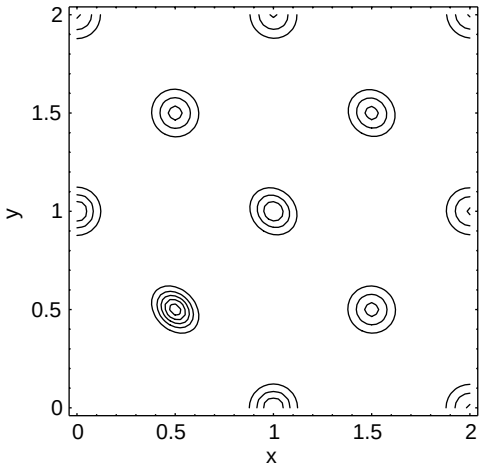

Fig. 3. Isolines of $g(\boldsymbol{r})$ for a classical fcc crystal at $\Gamma = 180$ in the plane shown in Fig. 1.

centered at these lattice sites. The peaks are high (the heights are as large as 30–40) and narrow, i.e., they do not overlap. The peak widths are determined by thermal vibrations of ions in their lattice sites. The plane at the bottom of each figure displays isolines of $g(\boldsymbol{r})$. Fig. 3 shows these isolines for the fcc crystal in more detail. The isolines for neighboring ions (close to the origin of coordinate system), are ellipsoidal, rather than circular. Thus, the ion–ion correlation properties depend on the direction of ion displacements. For more distant ions, the isolines become circular. For

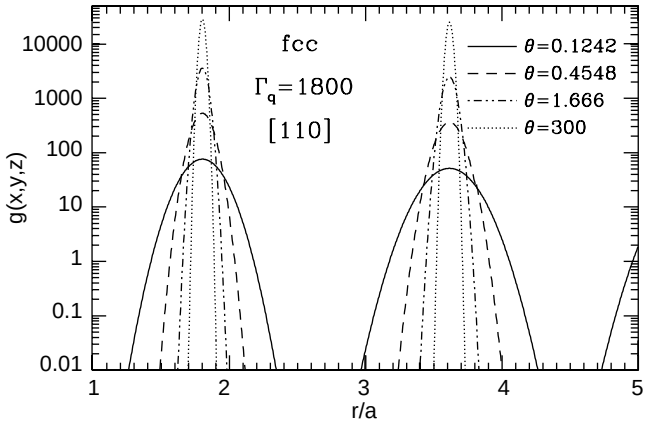

Fig. 4. $g(\boldsymbol{r})$ versus r in direction [1 1 0] for fcc crystal at $\Gamma_q = 1800$ and four values of θ.

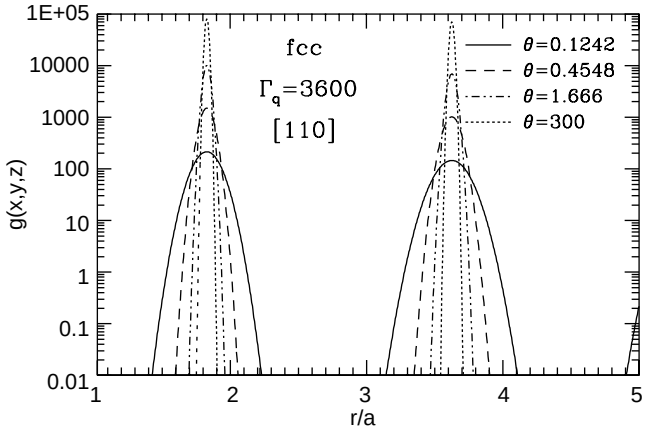

Fig. 5. Same as in Fig. 4 but at $\Gamma_q = 3600$.

these ions, the equality $v_{\alpha\beta}(\boldsymbol{R}) = v_0(\boldsymbol{R})\,\delta_{\alpha\beta}$ and associated Eq. (10) become a good approximation.

As long as the crystal remains classical ($\theta \lesssim 1$) the peak heights grow with Γ as $\propto \Gamma^{3/2}$, and the peak widths decrease as $\Gamma^{-1/2}$; the isoline ellipses decrease in size but remain selfsimilar. The situation becomes different for a quantum crystal.

A transition from classical to quantum crystals with decreasing temperature at a fixed number density of ions can be seen from Figs. 4–7. These figures exhibit $g(\boldsymbol{r})$ for fcc (Figs. 4 and 5) and bcc (Figs. 6 and 7) crystals at two values of the density parameter, $\Gamma_q = 1800$ (Figs. 4 and 6) and $\Gamma_q = 3600$ (Figs. 5 and 7). Each figure shows $g(\boldsymbol{r})$ as a function of r in units of a (the ion sphere radius) for a given Γ_q in one direction of $\boldsymbol{r}$ for four values of the quantum parameter: $\theta = 0.1242$, 0.4548, 1.666,

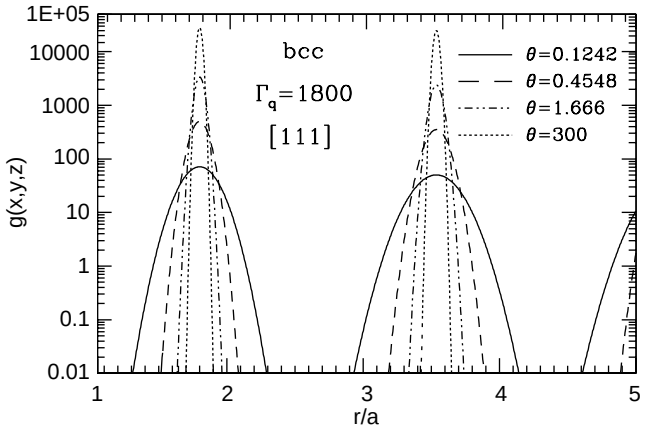

Fig. 6. $g(\boldsymbol{r})$ versus r in direction [1 1 1] for bcc crystal at $\Gamma_q = 1800$ and four values of θ.

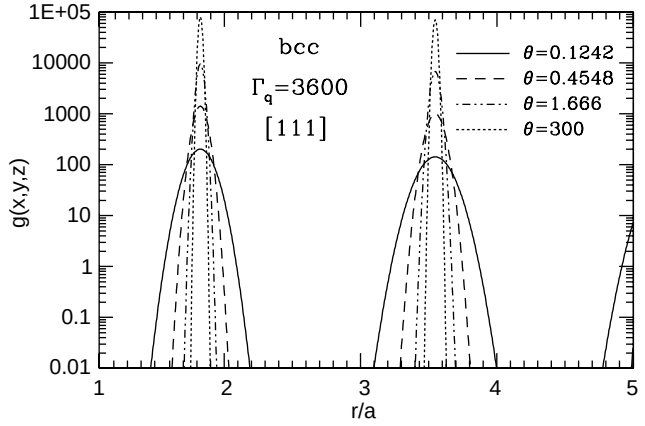

Fig. 7. Same as in Fig. 6 but at $\Gamma_q = 3600$.

and 300. The chosen directions of $\boldsymbol{r}$ lie in the planes displayed in Figs. 1 and 2. The lowest values of θ correspond to classical crystals while the highest θ corresponds to essentially quantum crystals. Logarithmic scale of $g(\boldsymbol{r})$ is used to show that the pair distribution varies with r by many orders of magnitude.

Consider, for instance, Fig. 4 which visualizes $g(\boldsymbol{r})$ along the direction $x = y$, $z = 0$. The solid line gives the pair distribution for the classical fcc crystal with $\Gamma = 220$, which does not differ strongly from that in Fig. 1. One can observe two closest correlation peaks and the wing of the third one. The peak heights reach the values ~ 100 and the peak widths are moderately small. In this classical regime, the pair distribution is actually determined by one parameter $\Gamma = \theta\Gamma_q$. Other lines correspond to a colder crystal of the same number density. The dashed line refers to $\Gamma \approx 820$. The crystal is

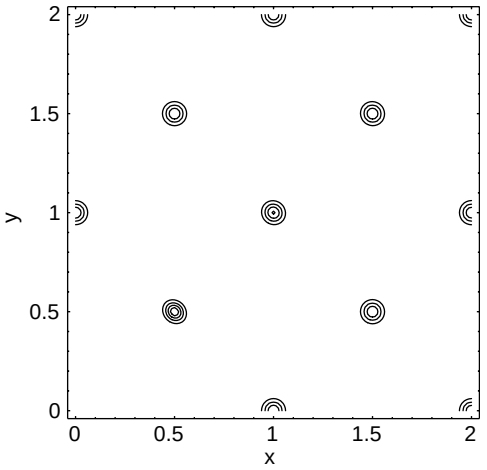

Fig. 8. Isolines of $g(\boldsymbol{r})$ for a fcc crystal in the plane shown in Fig. 1 but in the quantum regime ($T = 0$) at $\Gamma_q = 100$.

still classical; the peak heights reach the values ~500, and the peaks are noticeably narrower. The values of $g(\boldsymbol{r})$ outside the peaks are much smaller than for the solid line (not seen in the figure). The next, dash-and-dotted line refers to the intermediate classical–quantum regime, $\Gamma = 3000$. The peak heights are as large as ~3000, and the peaks are narrower. With further decrease of T (increase of θ) the peaks will become even higher and narrower, and we will enter the essentially quantum regime. In that regime, the rms ion displacements around the lattice sites are determined by zero-point ion vibrations, independent of temperature. The pair distribution becomes "frozen" (temperature independent) being solely determined by the density parameter Γ_q. The peak heights in this regime scale as $\Gamma_q^{3/2}$ and the peak widths scale as $\Gamma_q^{-1/2}$. This limiting pair distribution is shown by dots. The peak heights reach the values of ~30 000, and the peaks are very narrow. The pair distribution outside the peaks becomes extremely small. The isolines of $g(\boldsymbol{r})$ for such a case are plotted in Fig. 8 (for the fcc crystal in the same plane as in Fig. 1 but in the quantum regime). For a better presentation we have chosen the value $\Gamma_q = 100$. The isolines look more circular than in the classical crystal (cf. Fig. 3). Note in passing that $\Gamma_q = 100$ for a carbon plasma is realized at the density of 5.8×10^5 g cm^{-3}, which is a typical density in the cores of white dwarfs and the outer envelopes of neutron stars.

Fig. 5 shows the same pair distribution as in Fig. 4 but for a lower number density of ions (for higher $\Gamma_q \propto n^{-1/6}$). The main features are the same. Since the density is lower, zero-point ion vibrations are less pronounced and the peak heights of the pair distribution in the frozen quantum regime (the dotted line) are even higher, reaching the values ~10^5. The peak heights in the classical regime are solely determined by the value of $\Gamma = \Gamma_q\theta$ (not Γ_q, see above). Thus the difference of peak heights in the classical regime in different figures is caused by the difference of the values of Γ for

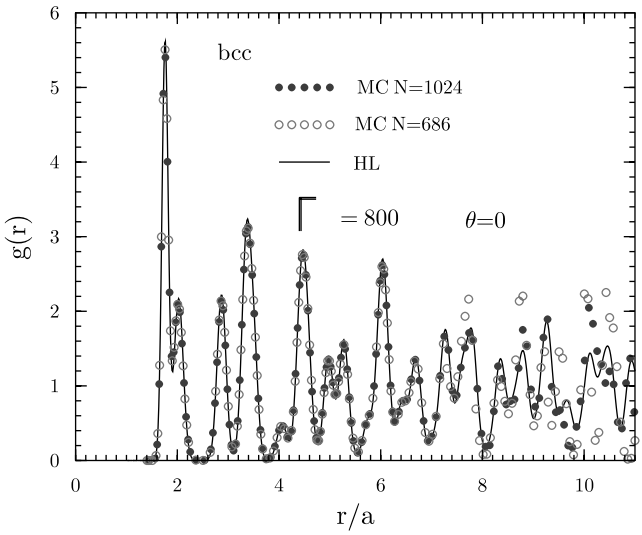

Fig. 9. $g(r)$ for a classical bcc Coulomb crystal at $\Gamma = 800$. Filled dots: MC with $N = 1024$ particles; open dots: MC with $N = 686$; solid line: HL.

different curves. Note that, contrary to Γ_q, $\Gamma \propto n^{1/3}$ decreases with decreasing density (at a fixed T).

Fig. 6 is similar to Fig. 4, but for the bcc lattice (in the direction in which $x = y = z$, at $\Gamma_q = 1800$). Fig. 7 corresponds to the same bcc crystal but for $\Gamma_q = 3600$; it is similar to Fig. 5. One can see that the main features of the pair distributions for the bcc and fcc lattices are the same.

4. Radial pair distribution

Now we focus on the properties of radial pair distribution function $g(r)$. First consider a classical Coulomb crystal, $\theta \to 0$, for which extensive MC simulations have been performed. The MC method is described, e.g., in Ref. [8].

Fig. 9 shows three sets of calculated $g(r)$ data for $\Gamma = 800$. The solid line represents the HL curve. One can clearly observe the correlation peaks accumulated from all directions of $\boldsymbol{r}$. Particularly, they come from direction [1 1 1] displayed in Fig. 6 (the appropriate $g(\boldsymbol{r})$ in Fig. 6 is shown by the dashed line; it corresponds to the classical crystal at $\Gamma \approx 820$). The peak heights of $g(r)$ are naturally much lower than the peak heights of $g(\boldsymbol{r})$ because of averaging over directions of $\boldsymbol{r}$.

Open circles in Fig. 9 exhibit MC data obtained with $N = 686$ particles over nearly 10^8 MC configurations already reported in Ref. [11]. The MC results for $g(r)$ are limited to half the size of the basic cell containing the N charges due to the bias from particles in the image cell adjacent to the basic cell. For $N = 686$, the basic cell length is about $14.2a$. Accordingly, the MC $g(r)$ for this simulation is valid only out

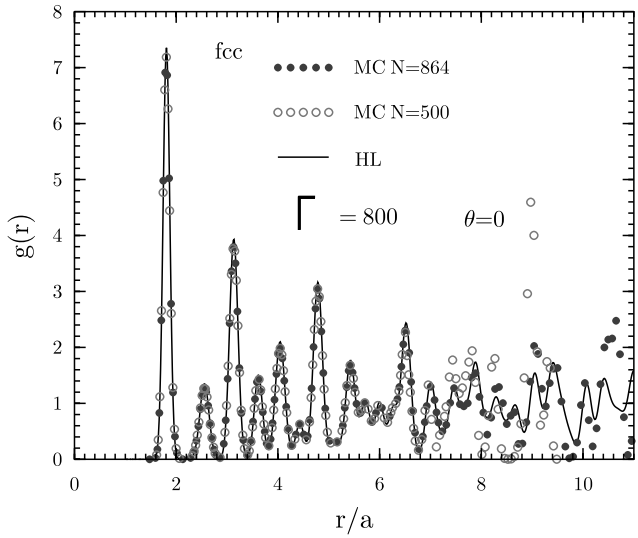

Fig. 10. $g(r)$ for a classical fcc Coulomb crystal at $\Gamma = 800$. Filled dots: MC with $N = 864$; open dots: MC with $N = 500$; solid line: HL.

to $r \approx 7.3a$ while $g(r)$, given by the HL model, remains accurate as $r \to \infty$. However, as discussed in Ref. [11], at small particle separations, $r \lesssim 1.5a$, the HL model is less accurate than MC (and MC data are available down to $r \gtrsim 1.1a$). Filled circles in Fig. 9 show our new MC $g(r)$ obtained with $N = 1024$ particles. As expected, larger N extends the validity of MC results from $r \approx 7.3a$ to $8.3a$.

Fig. 10 is similar to Fig. 9 but displays $g(r)$ for fcc Coulomb crystal. We present the results of our two MC runs obtained with $N = 500$ and 864. In the first case, the MC $g(r)$ is accurate at $r \lesssim 6.4a$ while in the second case it is accurate to about $r \lesssim 7.7a$. The peak positions are different from those in Fig. 9 due to different lattice structure. The peaks for fcc lattice are slightly more pronounced than those for bcc lattice.

Figs. 11–14 present HL $g(r)$ calculated for bcc (Figs. 11 and 12) and fcc (Figs. 13 and 14) for two values of the density parameter: $\Gamma_q = 1800$ (Figs. 11 and 13) and 3600 (Figs. 12 and 14). Each figure shows the curves which correspond to four values of the quantum parameter θ. These figures can be directly compared with Figs. 4–7 which display $g(\boldsymbol{r})$ for the same values of Γ_q and θ. The behavior of $g(r)$ in Figs. 11–14 is qualitatively similar. Under the same conditions (the same Γ_q and θ) the peaks of $g(r)$ for fcc are slightly higher than for bcc (in agreement with Figs. 9 and 10). The solid curves ($\theta = 0.1242$) are very close to those for classical Coulomb crystals (with $\Gamma = 224$ in Figs. 11 and 13, and $\Gamma = 447$ in Figs. 12 and 14).

Comparing the solid, dashed, dot-and-dashed, and dotted curves in each figure one can follow the evolution of $g(r)$ with increasing θ, i.e., decreasing temperature (at a given density) during transition from a classical to a quantum crystal. The evolution reflects the evolution of $g(\boldsymbol{r})$ described in Section 3. In the course of this transition, the peaks are seen to become higher and narrower which is associated with decreasing rms

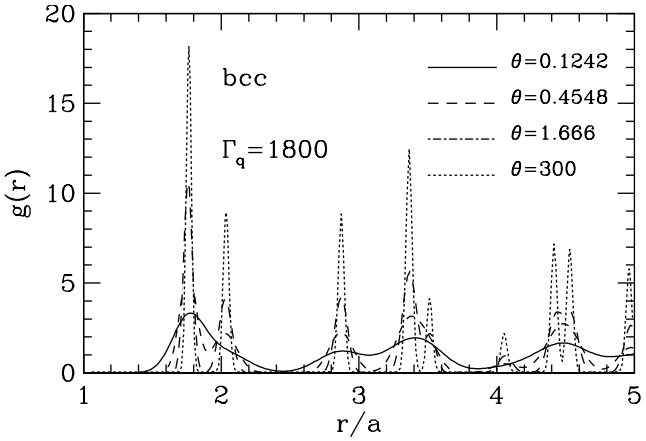

Fig. 11. $g(r)$ for a bcc Coulomb crystal at $\Gamma_q = 1800$ and four values of $\theta = 0.1242$, 0.4548, 1.666, and 300.

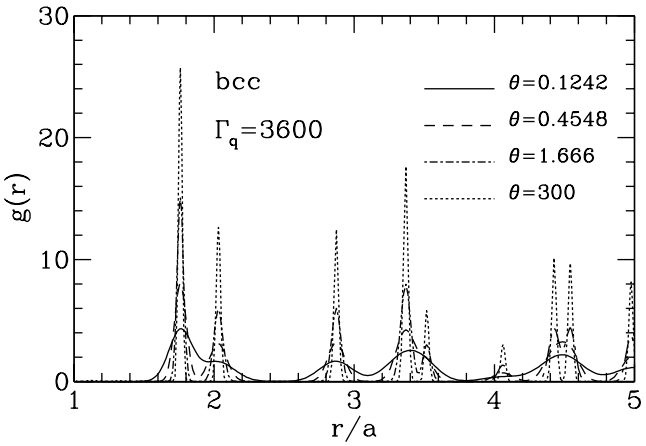

Fig. 12. Same as in Fig. 11 but at $\Gamma_q = 3600$.

amplitude, r_T, of ion vibrations in a lattice. In the classical regime, the peak heights evolve as $\sqrt{\Gamma}$, and the peak widths as $\Gamma^{-1/2}$. The highest $\theta = 300$ corresponds to the purely quantum crystal. In the latter case $g(r)$ is independent of T (or θ) and describes the "frozen" ($T = 0$) pair distribution determined by zero-point lattice vibrations alone. The peaks acquire their maximum heights and minimum widths (the heights behave as $\sqrt{\Gamma_q}$ and the widths as $\Gamma_q^{-1/2}$). Outside the peaks $g(r)$ is nearly zero.

If we decrease the number density of ions (equivalently, increase Γ_q; cf. Figs. 11 and 12; and also Figs. 13 and 14) the quantum peaks become higher and narrower [just as for $g(\boldsymbol{r})$]. On the contrary, if we were to increase the number density of ions the peaks in the quantum regime would become smaller and broader. At very high densities

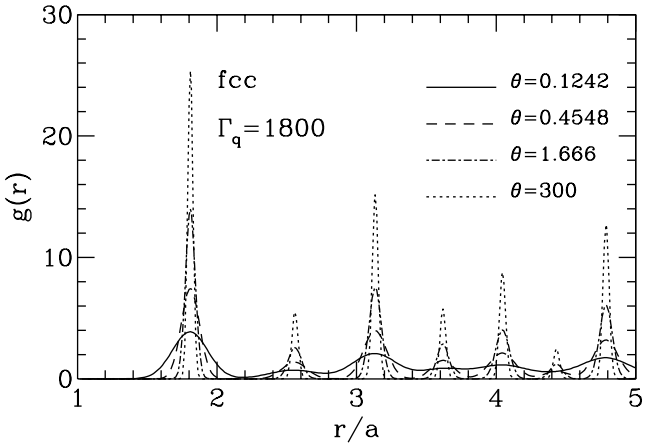

Fig. 13. $g(r)$ for a fcc Coulomb crystal at $\Gamma_q = 1800$ and $\theta = 0.1242$, 0.4548, 1.666, and 300.

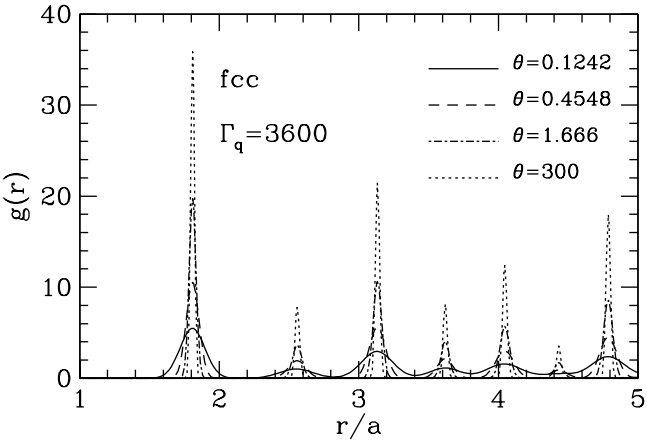

Fig. 14. Same as in Fig. 13 but for $\Gamma_q = 3600$.

they would start overlapping. We expect that, under these conditions, our consideration would fail because the exchange effects which we ignore would become important. Note that under these conditions zero-point ion vibrations may become sufficiently strong to prevent the appearance of crystal from Coulomb liquid (see, e.g., Ref. [3]).

Let us emphasize once more the simplicity of the HL model which allows us to calculate $g(\boldsymbol{r})$ and $g(r)$ to very large r using very modest computer resources. For instance, in Fig. 15 we present HL $g(r)$ for fcc crystal at $\Gamma = 800$ and two values of $\theta = 0.1$ (classical regime) and 10 (quantum regime) evaluated up to $r = 400a$. One can observe a pronounced peak structure even for $r \sim 400a$ but the peak heights decrease gradually with r. The classical peaks are naturally higher and narrower. We

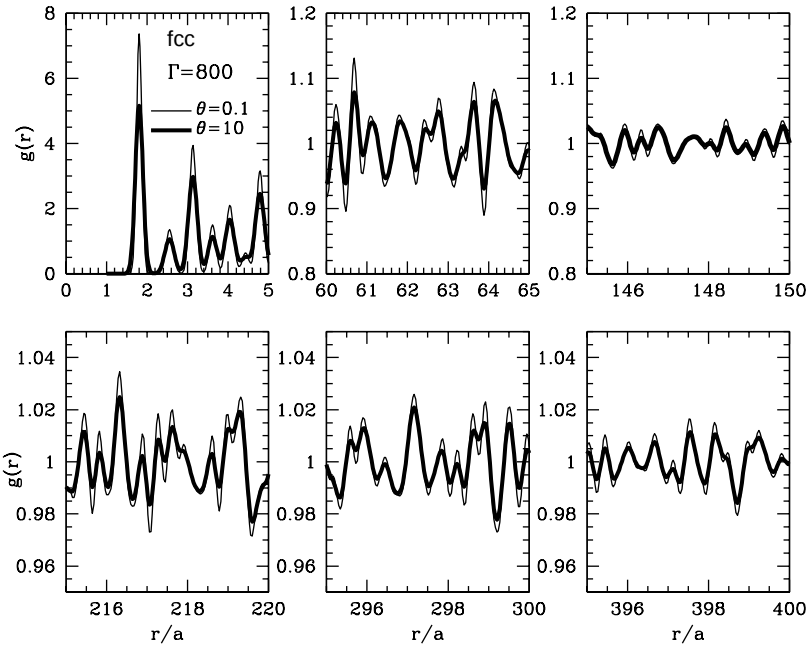

Fig. 15. Radial pair distribution function of an fcc crystal at $\Gamma = 800$ and $\theta = 0.1$ (thin lines) and 10 (thick lines) in six intervals of r up to $r = 400a$.

have checked that in all the panels of Fig. 15 but the upper left panel ($r \leqslant 5a$) $g(r)$ is accurately reproduced assuming that distant ions vibrate independently in their lattice sites (which is equivalent to $v_{\alpha\beta}(\boldsymbol{R}) = 0$, $V_0(\boldsymbol{R}) = r_T^2/3$ in the equations of Section 2). Thus the pair distribution at large r is fairly simple. For the conditions displayed in Fig. 15 the approximation of independent ion vibrations becomes very accurate at $r \gtrsim 20a$.

5. Conclusions

We have calculated the pair-distribution functions $g(\boldsymbol{r})$ and $g(r)$ in the HL approximation for bcc and fcc Coulomb crystals in a wide temperature range, from the classical high-temperature regime ($\theta \ll 1$) to the quantum low-temperature regime ($\theta \gg 1$). In the classical regime, we have compared the HL $g(r)$ with the results of MC calculations at different numbers of ions N. We find a very good agreement of MC and HL results and show that increasing N used in MC runs makes this agreement better.

Using the HL $g(\boldsymbol{r})$ and $g(r)$, we have shown that with decreasing temperature the peaks of the pair distribution become higher and narrower, and they finally "freeze" in the quantum regime being solely determined by zero-point ion vibrations.

Let us stress that the quantum effects cannot be taken into account in a classical MC scheme. In principle, they may be explored using PIMC but such studies require

very powerful computers. At present, the HL model gives the only simple method to explore ion correlations in quantum Coulomb crystals. Equally, the HL model is the only one which gives accurate values of $g(\boldsymbol{r})$ for any crystal-vibration regime, classical or quantum. In addition, we would like to stress the simplicity of the HL method. It allows one to study not only static correlations but also dynamical effects [11] important in thermodynamics and kinetics of Coulomb crystals (Section 1) as well as ion correlations in a crystal in the presence of a magnetic field.

Acknowledgements

The work of AIC and DGY was supported in part by RFBR (grants 02-02-17668 and 00-07-90183). The work of HEDW and WLS was performed under the auspices of the US Department of Energy under contract number W-7405-ENG-48 for the Lawrence Livermore National Laboratory and W-7405-ENG-36 for the Los Alamos National Laboratory.

References

[1] S.Ya. Rakhmanov, Zh. Eksp. Teor. Fiz. 75 (1978) 160.
[2] W.M. Itano, J.J. Bollinger, J.N. Tan, B. Jelenković, X.-P. Huang, D.J. Wineland, Science 279 (1998) 686;
D.H.E. Dubin, T.M. O'Neil, Rev. Mod. Phys. 71 (1999) 87.
[3] G. Chabrier, Astrophys. J. 414 (1993) 695;
G. Chabrier, N.W. Ashcroft, H.E. DeWitt, Nature 360 (1992) 48.
[4] E.E. Salpeter, H.M. Van Horn, Astrophys. J. 155 (1969) 183;
S. Schramm, S.E. Coonin, Astrophys. J. 365 (1990) 296.
[5] D.A. Baiko, D.G. Yakovlev, Astron. Lett. 21 (1995) 702.
[6] D.A. Baiko, A.D. Kaminker, A.Y. Potekhin, D.G. Yakovlev, Phys. Rev. Lett. 81 (1998) 5556.
[7] A.Y. Potekhin, D.A. Baiko, P. Haensel, D.G. Yakovlev, Astron. Astrophys. 346 (1999) 345.
[8] G.S. Stringfellow, H.E. DeWitt, W.L. Slattery, Phys. Rev. A 41 (1990) 1105;
W.L. Slattery, G.D. Doolen, H.E. DeWitt, Phys. Rev. A 21 (1980) 2087.
[9] R.T. Farouki, S. Hamaguchi, Phys. Rev. E 47 (1993) 4330.
[10] S. Ogata, Astrophys. J. 481 (1997) 883.
[11] D.A. Baiko, D.G. Yakovlev, H.E. DeWitt, W.L. Slattery, Phys. Rev. E 61 (2000) 1912.
[12] A.A. Maradudin, E.W. Montroll, G.H. Weiss, Theory of Lattice Dynamics in the Harmonic Approximation, Academic Press, New York, 1963.
[13] R.C. Albers, J.E. Gubernatis, preprint, LASL LA-8674-MS, 1981.
[14] H. DeWitt, W. Slattery, D. Baiko, D. Yakovlev, Contrib. Plasma Phys. 41 (2001) 251.